Propagation of Slow Slip Events on Rough Faults: Clustering, Back Propagation, and Re-rupturing

Yudong Sun[1] **and Camilla Cattania**[1]

[1]Department of Earth, Atmospheric, and Planetary Sciences, Massachusetts Institute of Technology, Cambridge, MA, USA

Key Points:

- Slow slip events on a simulated rough fault exhibit clustering, a broad range of rupture lengths, and varying propagation velocities
- Fast back-propagating fronts arise from the interplay of strength heterogeneity, variable slip rate, and rate-strengthening friction
- A transition from pulse to crack can also lead to the re-rupture of slow slip events on a fractal fault

Corresponding author: Yudong Sun, yudong@mit.edu

Abstract

Seismic and geodetic observations show that slow slip events (SSEs) in subduction zones can happen at all temporal and spatial scales and propagate at various velocities. Observation of rapid tremor reversals (RTRs) indicates back-propagating fronts traveling much faster than the main rupture front. Heterogeneity of fault properties, such as fault roughness, is a ubiquitous feature often invoked to explain this complex behavior, but how roughness affects SSEs is poorly understood. Here we use quasi-dynamic seismic cycle simulations to model SSEs on a rough fault, using normal stress perturbations as a proxy for roughness and assuming rate-and-state friction, with strengthening behavior at high slip rate. SSEs exhibit temporal clustering, large variations in rupture length and propagation speed, and back-propagating fronts at different scales. We identify a mechanism for back propagation: as ruptures propagate through low-normal stress regions, a rapid increase in slip velocity combined with rate-strengthening friction induces stress oscillations at the rupture tip, and the subsequent "delayed stress drop" induces secondary back-propagating fronts. Moreover, on rough faults with fractal elevation profiles, the transition from pulse to crack can also lead to the re-rupture of SSEs due to local variations in the level of heterogeneity. Our study provides a possible mechanism for the complex evolution of SSEs inferred from geophysical observations and its link to fault roughness.

Plain Language Summary

Aseismic slow slip events (SSEs), which like earthquakes can accommodate plate motions, are observed to happen intermittently, propagate backward, and travel at varying speeds. The rough geometry of faults causes heterogeneous stress distribution, which may be responsible for the complex slip behaviors. Here we use computer simulations and analytical tools to study the propagation of SSEs on rough faults. We find more small SSEs, occurring in short bursts, on a rougher fault. We also reproduce faster back-propagating streaks in simulations, analogous to seismological observations. On a fractal fault, ruptures can transition between slip modes (from inchworm-like to zipper-like) which further induces re-rupturing when propagating from high to low roughness areas. Our study helps quantify the effect of fault roughness and further understand underlying mechanics.

1 Introduction

Slow slip events are aseismic fault slip transients with a slip rate of about $1-100$ mm/day (Wech & Bartlow, 2014; Hawthorne et al., 2016; Bletery et al., 2017; Frank et al., 2018; Bletery & Nocquet, 2020). Slow slip events (SSEs) and non-volcanic tremors have been observed worldwide in subduction zones, such as Cascadia, Nankai, and Hikurangi (Rogers & Dragert, 2003; Obara et al., 2004; Wallace, 2020). Several candidate mechanisms for slow slip events have been proposed, such as localized regions of lower normal stress (Liu & Rice, 2005, 2007; Rubin, 2008), fault gouge dilatancy (Segall & Rice, 1995; Segall et al., 2010), a transition to velocity-strengthening at a high slip rate (Hawthorne & Rubin, 2013a; Im et al., 2020), and frictional fault embedded within a viscous shear zone (Lavier et al., 2013; Yin et al., 2018; Behr et al., 2021).

Slow slip events exhibit remarkable spatio-temporal complexity. Frank (2016) and Frank et al. (2018) reveal smaller SSEs hidden within the interseismic periods and large events, respectively (also see Rousset et al. (2019)). They also find SSEs are clustered, similar to a cascade of aftershocks following the mainshock (Jolivet & Frank, 2020). Jolivet et al. (2015) and Hawthorne and Bartlow (2018) suggest that the moment of SSEs follows a power law distribution, which resembles Gutenberg-Richter law. The rupture style of SSEs, and the magnitude-duration scaling, are still subjects to debate. SSEs from different regions show a linear moment-duration scaling (Peng & Gomberg, 2010; Gao et

al., 2012), associated with pulse-like rupture along an elongated fault (as inferred by Bartlow et al. (2011) and Radiguet et al. (2011)). On the other hand, events from a single region follow a duration-cubed scaling like earthquakes (Michel et al., 2019), reminiscent of crack-like propagation.

With advances in seismic and geodetic observations, uncommon slow slip behaviors have been identified, and propagation velocities have been better measured. Wech and Bartlow (2014) use GPS measurement and locations of tremors to find that SSEs can rupture the same region again with a gap of about 3 weeks by bifurcating into bilateral propagation fronts in Cascadia. Yamashita et al. (2015) observe a re-rupturing event represented by migrating tremors several days after the first event in the Nankai subduction zone. Houston et al. (2011) and Obara et al. (2012) observed even faster back-propagating streaks represented by rapid tremor reversals (RTRs) in the Cascadia, and Nankai subduction zones, which have also been confirmed with borehole strainmeters (Hawthorne et al., 2016) and analysis of low-frequency earthquakes (Bletery et al., 2017).

These complex slip patterns are likely a manifestation of frictional behavior, fault heterogeneity, or the interplay between the two. As such, they offer an opportunity to understand the underlying physical mechanism for slow slip events and constrain fault properties in the environment of SSEs. Previous models incorporating heterogeneity typically assume spatial variations in frictional properties: velocity weakening (VW) asperities embedded in a velocity strengthening (VS) fault, producing localized stick-slip behavior on a creeping fault (e.g., Luo and Liu (2021)). Other studies employ a velocity-cutoff model with a transition from velocity weakening to velocity strengthening behavior with increasing slip rate and introduce heterogeneity by varying the cutoff-velocity (Peng & Rubin, 2018). While the existence of mixed-mode behavior at depths corresponding to SSEs is supported by observations (Behr & Bürgmann, 2021; Kirkpatrick et al., 2021), their spatial distribution is not well constrained, and modeling studies have approximated them by placing asperities at random locations, or on a grid (Peng & Rubin, 2018; Luo & Ampuero, 2018). Additionally, several mechanisms have been proposed to explain back propagation and rapid tremor reversals, such as tidal modulation (Hawthorne & Rubin, 2013b), fluid pressure wave (Cruz-Atienza et al., 2018; Yin, 2018), fault heterogeneity (Luo & Ampuero, 2018; Luo & Liu, 2021), and fault damage zone (Idini & Ampuero, 2020).

Fault roughness represents a ubiquitous and well-characterized source of heterogeneity, and like other heterogeneities described above, it can modulate fault stability (Cattania & Segall, 2021). The migrations of tremors in the Nankai subduction zone exhibit spatial variations of predominant directions (either along strike or dip), as shown in Sagae et al. (2023). This implies that structural heterogeneities, like fault roughness, play a significant role due to their known anisotropic properties (Renard & Candela, 2017), rather than just material differences. Furthermore, it is well established that fault roughness controls the spatial distribution of fault normal stresses (Fang & Dunham, 2013; Romanet et al., 2020; Cattania & Segall, 2021), and the effect of normal stress perturbations depends on the ratio of normal stress perturbations to background effective normal stress. Due to the low normal stress conditions associated with SSEs, the change of normal stress due to fault roughness may play an important role in controlling their behavior, making them an ideal setting in which to study the effect of heterogeneity on fault slip patterns. In this study, we seek to determine the effect of fault roughness on the complex rupture behaviors during SSEs. We use numerical simulations and fracture mechanics to address the following question: Can fault roughness explain the spatio-temporal variety of SSE behavior, back propagation, and re-rupture?

After introducing the modeling framework (Section 2), we consider the simple case of sinusoidal perturbations in normal stress (Section 3.1) and show that heterogeneity with small wavelength and large amplitudes favors complex slip behaviors including a variety of rupture dimension, clustering, and forward and backward, fast and slow prop-

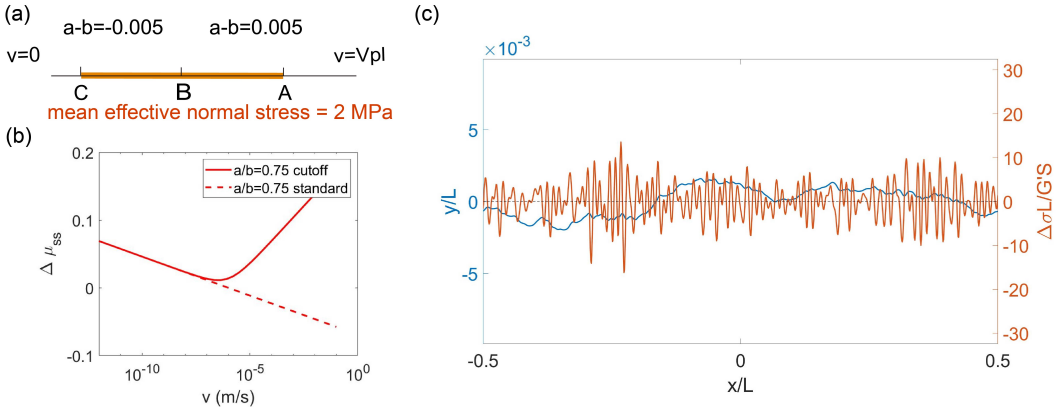

Figure 1. (a) Model geometry. (b) The steady-state friction coefficient of the original rate-and-state friction (dashed line) and velocity cutoff model (solid line, Equation 2). (c) An example of normalized elevation of a rough fault y/L (blue) and perturbation of the normal stress per slip $\Delta\sigma L/G'S$ (red) obtained from Equation 4.

agation. Furthermore, we introduce an analytical tool based on fracture mechanics to explain why SSEs arrest or propagate on a fault with variable normal stress. In Section 3.2, we discuss a possible mechanism to generate fast-moving back-propagating fronts: a delayed stress drop induced by the coupling between normal stress heterogeneity and friction. Finally, in Section 3.3 we consider a fractal fault, and demonstrate that its irregular distribution of normal stresses produces dynamics that are not captured by the sinusoidal model. In particular, we demonstrate SSE re-rupturing can be induced by a transition between the pulse to crack-like rupture, as the rupture propagates through regions of variable local roughness amplitude.

2 Models

We use the 2D quasi-dynamic boundary element model FDRA (Segall & Bradley, 2012) to simulate SSE cycles on a rough fault. We include normal stress perturbations as proxies for roughness due to its lower computation cost. The evolution of normal stress and fault geometry is not considered in this study. Thus, our simulations can be thought as freeze-frame in the tectonic time scale. This simplification is justified because normal stress perturbations grow linearly with slip, and a single SSE only increases the total slip by a small fraction, so that normal stress perturbations do not change significantly during several cycles.

The model consists of an in-plane fault (mode II) in full space with velocity boundary conditions of tectonic loading rate v_{pl} and 0 at A and C, respectively (Figure 1a; Table 1), representing the region between the locked seismogenic zone and steady creep, where deep SSEs have been observed (Obara et al., 2004; Rogers & Dragert, 2003; Lay et al., 2012). The fault is composed of a shallow seismogenic (velocity-weakening) region, BC, and a deep creeping (velocity-strengthening) region, AB. Fault slip is governed by:

$$\tau_{el} = \tau_f + \frac{G}{2c_s} v, \tag{1}$$

where τ_{el} is the shear stress due to remote loading and interaction between elements, τ_f is the frictional resistance, and $\frac{G}{2c_s}v$ is the radiation damping term with shear wave velocity c_s and shear modulus G (Rice, 1993). Slow slip events on a velocity weakening fault require a stabilizing mechanism, such a reduction in pore pressure due to slip-induced

Table 1. Model parameters

parameter	value
fault length L	2.5 or 10 km
tectonic loading rate v_{pl}	1×10^{-9} m/s
shear modulus G	3×10^{10} Pa
Poisson's ratio ν	0.25
S wave velocity c_s	3.7×10^{3} m/s
friction coefficient μ_0	0.6
reference slip rate v^*	1×10^{-6} m/s
cut-off slip rate v_c	1×10^{-6} m/s
slip rate $v_{\tau-min}$ with minimum steady-state friction	3.33×10^{-7} m/s
friction parameter a for velocity-weakening region	0.015
friction parameter a for velocity-strengthening region	0.025
friction parameter b	0.02
characteristic slip distance D_c	4×10^{-5} m
average normal stress σ_0	2 MPa
amplitude-to-wavelength ratio α_r	0.001
Hurst exponent H	0.7

dilatancy (Segall & Rice, 1995) or a transition to velocity strengthening friction with increasing slip velocity, demonstrated in laboratory experiments (Saffer et al., 2001; Ikari & Saffer, 2011). Here we assume the latter mechanism and employ the velocity-cutoff model introduced by Hawthorne and Rubin (2013a). Frictional resistance is given by:

$$\tau_f = \left[\mu_1 + a \ln \frac{v}{v^*} + b \ln \left(\frac{\theta v_c}{D_c} + 1\right)\right] \sigma, \tag{2}$$

where $\sigma, \mu_1, v, v^*, \theta, D_c$ and v_c represent normal stress, reference frictional coefficient, slip rate, reference slip rate, state variable, characteristic slip distance, and cutoff velocity, respectively. a and b are the coefficients for instant and evolution effects. State evolution is governed by the aging law (Ruina, 1983) as:

$$\dot{\theta} = 1 - \frac{\theta v}{D_c}. \tag{3}$$

In contrast, the original rate-and-state friction is $\mu = \mu_0 + a \ln \frac{v}{v^*} + b \ln \frac{\theta v^*}{D_c}$. To match two frictional laws at low slip rate, we set μ_1 as $\mu_0 + b \ln \frac{v^*}{v_c}$ (Equation 2). As shown in Figure 1b, the steady-state friction $\mu_{ss} = \mu_1 + a \ln \frac{v}{v^*} + b \ln(\frac{v^*}{v} + 1)$ decreases to a minimum when v reaches $v_{\tau-min} = \frac{b-a}{a} v_c$, and then increases with increasing slip rate, so that slip instability initiates at $v < v_{\tau-min}$ and does not accelerate into an earthquake (Figure 1b).

The friction parameters a, b, D_c and average normal stress σ_0 we use are shown in Table 1 and consistent with previous studies (Marone, 1998; Liu & Rice, 2007; Audet & Kim, 2016). The mean normal stress σ_0 used in the simulations is 2 MPa, which makes the stress drop $\Delta\tau_{drop}$ about 0.1 MPa, within the range of 0.01 to 1 MPa, consistent with those inferred by Gao et al. (2012). We impose a perturbation of normal stress, which mimics the stress heterogeneity on a rough fault with a constant wavelength or a fractal distribution (e.g. Figure 1c). We refer to patches of elevated normal stress as asperities throughout the paper. We set the minimum grid spacing to $\frac{1}{2.5}$ of the smallest cohesive zone size L_c to adequately resolve the stress field across the crack tip (Erickson et al., 2023). The size of cohesive zone L_c is estimated as $1.377 \frac{G' D_c}{b \sigma_{max}}$ (Rubin & Ampuero, 2005), where σ_{max} and G' are the maximum normal stress and $\frac{G}{1-\nu}$, respectively.

We use synthetic fractal fault profiles, comparable to natural faults. Faults are corrugated at all scales, and the distribution is self-affine with a Hurst exponent H between $0.4-0.8$ (W. Power et al., 1987; Candela et al., 2012; Brodsky et al., 2016; Renard & Candela, 2017). The fractal fault topography has a power spectrum P^2 proportional to $(2\pi\lambda)^{-2H-1}$, where λ is the wavelength, and the root-mean-square elevation is given by $y_{RMS} = \alpha_r \lambda_{max}^H$, where α_r is the amplitude-to-wavelength ratio and λ_{max} is the maximum wavelength. For instance, Figure 1c shows a fractal fault with a normalized wavelength λ/L from 0.01 to 1 and $\alpha_r = 0.001$. We use the following analytical expressions to relate normal stress perturbations to fault topography (Fang & Dunham, 2013; Cattania & Segall, 2021):

$$\Delta\sigma(x) = \frac{G'S}{2}\mathscr{H}(y'') = \frac{G'S}{2}\int_{-\infty}^{\infty}\frac{y''(\xi)}{x-\xi}d\xi, \tag{4}$$

where S is the total slip, and additional shear stress is given by $\Delta\tau(x) = \frac{G'S}{2}y'\mathscr{H}(y'')$, where $\mathscr{H}(y'')$ is the Hilbert transform of the second derivative of the elevation amplitude y, and S is the accumulated slip. This formula describes $\Delta\sigma$ increases linearly with S in the elastic regime and does not apply when S is large enough to cause plastic deformation or fracturing. The corrugation perturbs the normal stress and shear stress locally at the scale of the smallest wavelength λ_{min} (Fang & Dunham, 2013; Romanet et al., 2020; Cattania & Segall, 2021). The root-mean-square (RMS) of normal stress perturbation is $\Delta\sigma_{RMS} = (2\pi)^2\alpha_r\sqrt{\frac{H}{2-H}}\frac{G'S}{2}\lambda_{min}^{H-2}$. While the mean of $\Delta\tau$ is $\Delta\tau_{mean} = (2\pi)^3\alpha_r^2\frac{2H}{3-2H}\frac{G'S}{2}\lambda_{min}^{2H-3}$, which is proportional to α_r^2 while $\Delta\sigma_{RMS}$ is proportional to α_r. The amplitude-to-wavelength ratio α_r of natural faults is about 10^{-3} to 10^{-2} (W. L. Power & Tullis, 1991). Therefore, we only consider the roughness-induced normal stress perturbation $\Delta\sigma$ but not the shear stress $\Delta\tau$ because it is much smaller than $\Delta\sigma$. We use a slip rate threshold to identify SSEs and to estimate propagation velocities for individual ruptures and cascading clusters (more detail is provided in section Appendix A).

3 Results

To obtain insight into how roughness affects slow slip behavior, we first explore the simple case of sinusoidal perturbations with varying wavelengths and amplitudes; in Section 3.3 we consider the more realistic case of normal stresses induced by slip on a fractal fault.

3.1 Variety of slip behavior on a sinusoidal rough fault

We consider a rough fault with a sinusoidal normal stress distribution with a magnitude given by

$$\sigma(x) = \sigma_0 + \sigma_A \cos\frac{2\pi x}{\lambda}. \tag{5}$$

Simulations exhibit a range of SSE behaviors, varying with both wavelength λ and amplitude of the normal stress perturbation σ_A. Figure 2 shows a slip behavior as a function of λ and σ_A/σ_0. To better highlight differences between simulations, we plot accumulated slip normalized by the theoretical slip profile or a crack driven by end-point displacement (in this case provided by deep creep), given by Rubin (2008):

$$S(x,t) = \frac{S(L,t)}{\pi}\left(\frac{\pi}{2} + \arcsin\frac{x-L/2}{L/2}\right), \tag{6}$$

where L, x, and t are the fault length, the location on the fault, and time. We choose a 2.5 km-long flat fault that is a few times larger than the nucleation length, so that it only has full ruptures in the homogeneous-σ case (see Cattania (2019)), as shown in Figure 2a and 2b. In this case, full ruptures are well approximated as a constant stress drop crack (Figure 2a), with an elliptical slip profile (Eshelby, 1957). Cases with low σ_A/σ_0

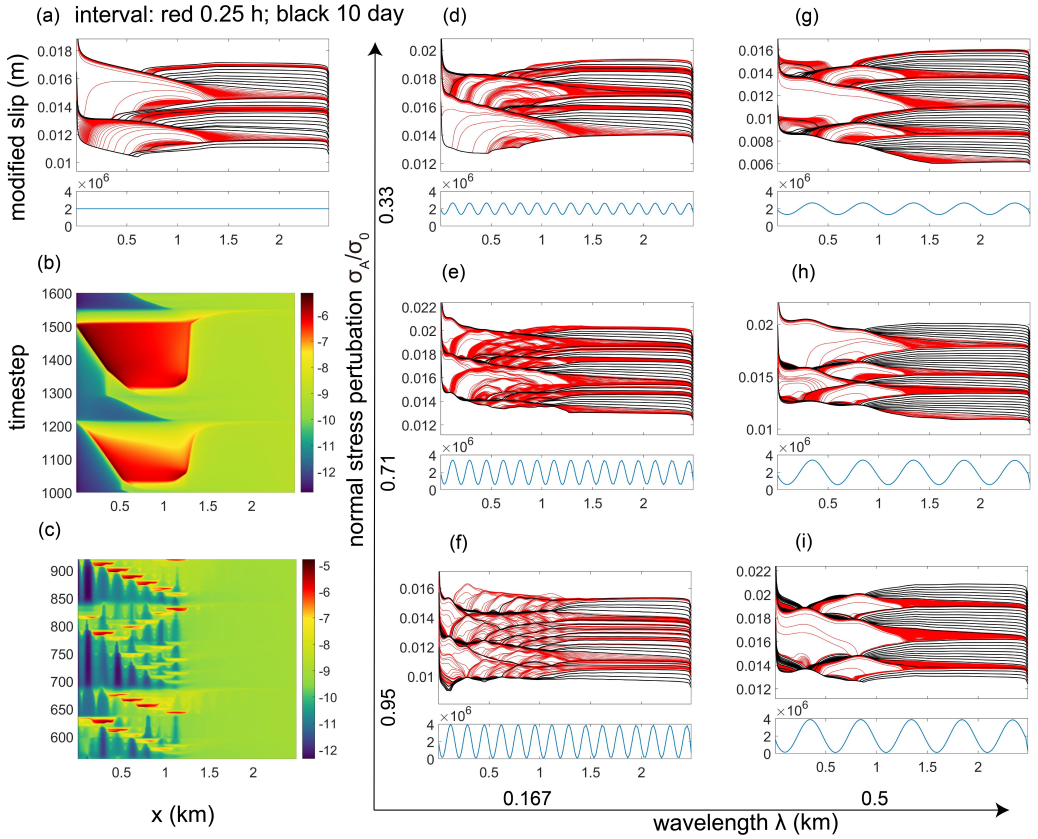

Figure 2. Effect of sinusoidal normal stress perturbations on rupture style. (a) normalized slips with uniform σ. Normalized slip equals slip s divided by $\frac{\pi}{2} + \arcsin\frac{x-W/2}{W/2}$. (d-i) Normalized slip profiles as a function of wavelength (λ) and perturbation amplitude (σ_A/σ_0). (b) and (c) show the slip rate for each time step for cases (a) and (f), respectively.

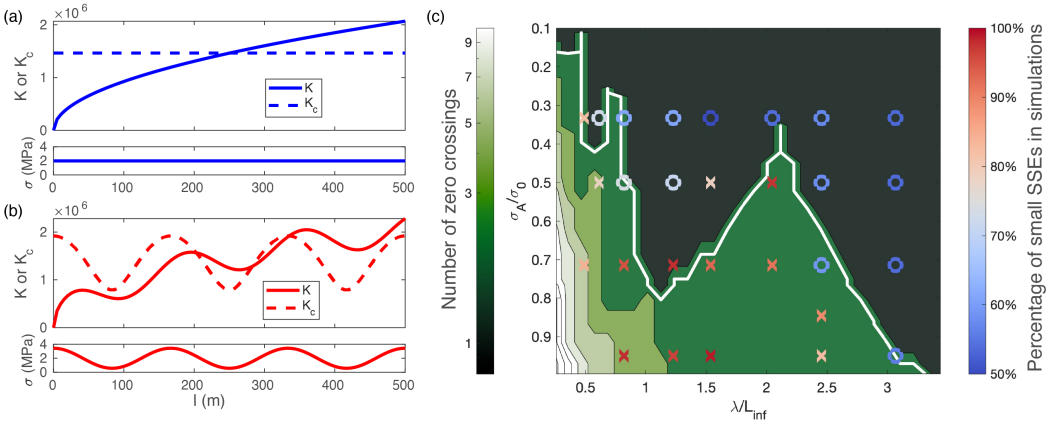

Figure 3. Stress intensity factor K (solid line) and local toughness K_c (dashed line) for the constant (a) and perturbed (b) normal stress. The slip will arrest at $l = 280$ m. (c) Number of zero crossings of $K - K_c$ and percentage of small SSEs in simulations with varying normalized wavelength λ/L_∞ and amplitude-to-constant ratio σ_A/σ_0. The red contouring line represents the threshold for arresting (3 zero crossings). Colors of circles and crosses represent the percentage of events smaller than 2λ in the simulations with a 2.5 km-long fault (circle: > 0.75; cross: < 0.75).

and long wavelength exhibit crack-like ruptures and partial ruptures (Figure 2d, 2g and 2h), whereas with the increase of wavenumber and perturbation amplitude σ_A, there are more pulse-like ruptures composed of localized slip pockets and an overall flat slip profile (Figure 2f). A similar transition from crack to pulse-like rupture due to fault roughness was observed by Heimisson (2020), and interpreted as a consequence of additional shear resistance from fault roughness (roughness drag; Fang and Dunham (2013)). Our results indicate that pulse-like rupture can still occur exclusively as a result of a perturbation in normal stress. Each cluster ruptures the whole velocity-weakening region intermittently, and it ruptures more than once in some regions (Figure 2c and 2f). Note that these partial ruptures are often nucleated at a high-σ region and arrested by the high-σ regions nearby (Figure 2f and 2i), which have a higher local fracture energy, as discussed below.

3.1.1 Rupture arrest with variable normal stress

To get more insight into rupture arrest, we use a fracture mechanics criterion accounting for heterogeneity. Rupture propagation is controlled by the criterion: $K = K_c$, where K and K_c are stress intensity factor and local toughness, respectively (Griffith, 1921; Irwin, 1957). Normal stress heterogeneity affects both these terms: enhanced compression at the crack tip increases the local toughness K_c, thus favoring rupture arrest; however, it also increases the stress drop and hence K, which promotes rupture propagation. Analytical calculations are described in Appendix B.

Figure 3a and b illustrate examples of K and K_c distributions for constant and perturbed normal stress. The zero crossing of $K - K_c$ of a smooth fault (red) is located at about $l \approx 250$ m, which is similar to the nucleation half length $L_\infty = \frac{G' b D_c}{\pi(b-a)^2\sigma}$. As the crack reaches the nucleation dimension, it will grow unstable and propagate indefinitely as long as the stress drop remains uniform. However, $K - K_c$ has 3 zero crossings for the case with perturbed normal stress (blue). The SSE is likely to nucleate at the first zero crossing ($l \approx 200$ m) and arrest at the second zero crossing ($l \approx 280$ m) because it cannot penetrate the high-σ region ($l \approx 280 - 330$ m) where $K < K_c$.

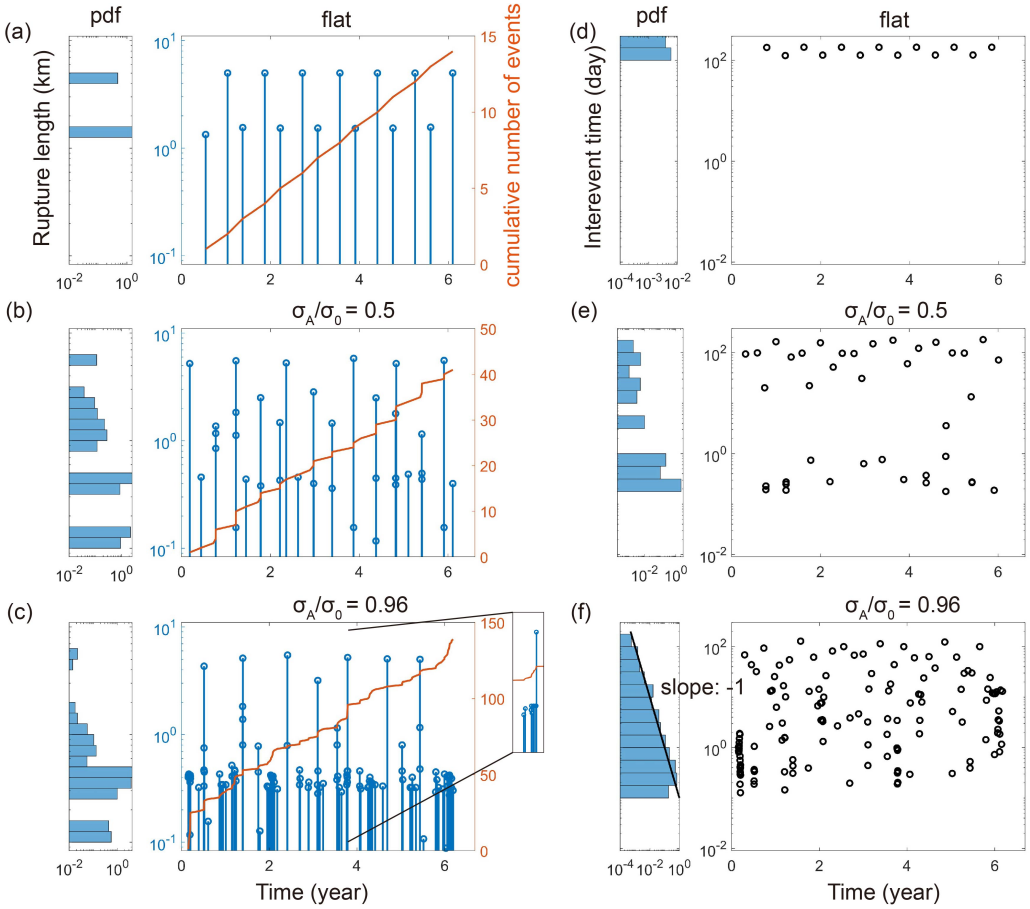

Figure 4. Effect of perturbation amplitude on SSE catalogs. Rupture lengths (a, b, c) and interevent times (d, e, f) with increasing sinusoidal σ perturbation on a 10 km-long fault ($\lambda = 0.33$ km). SSEs are outlined by a threshold of 1×10^{-6} m/s. Events that are closer than the duration of full ruptures are merged as one.

Figure 3c shows the conditions under which SSEs might arrest according to this analysis. Figure 3c excludes the perturbed wavelength shorter than the cohesive zone ($1.377L_b \approx 55$ m), with $L_b = \frac{G' D_c}{b\sigma}$ (Rubin & Ampuero, 2005; Ampuero & Rubin, 2008), because local toughness K_c cannot be calculated as Equation B4 due to the varying normal stress in the cohesive zone. If $K - K_c$ has more than three zero crossings in Figure 3b, the SSEs tend to stop at the high-normal-stress region and propagate like a pulse discontinuously. Therefore, the parameter space for arresting is below the white curve, while the black area indicates that ruptures will not arrest. For the same wavelength λ, SSEs are more likely to arrest if the normal stress perturbation is larger. The range of wavelength promoting rupture arrest is narrow for smaller normal stress perturbations. We also compare our analytical model with the percentage of SSEs smaller than 2λ in the simulations (several cases are shown in Figure 2) since there are more small SSEs if arresting happens more frequently. The cross indicates that most SSEs ($> 75\%$) are small, while the circle indicates fewer small ruptures ($< 75\%$). To first order, the distribution of crosses and circles shows a Z-shaped boundary and our model aligns with simulations. This analysis demonstrates that the strong spatial variations of both local toughness K_c and stress intensity factor K of potential ruptures along the rough fault can account for the breakdown of a single large SSE into multiple smaller SSEs.

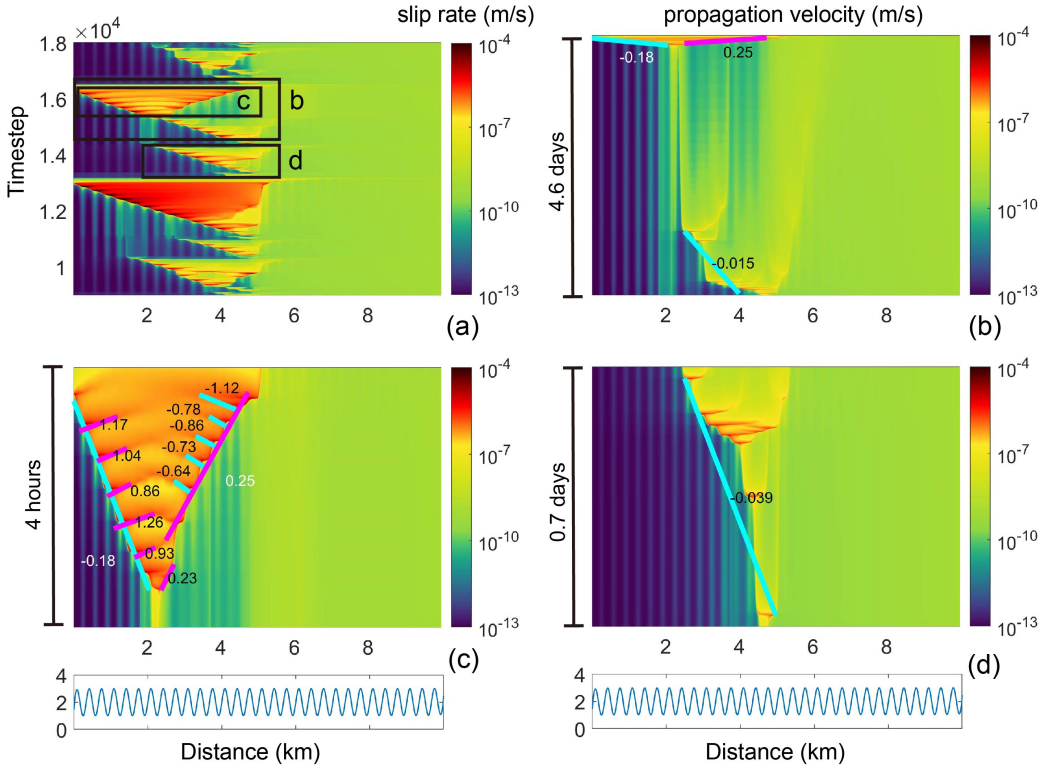

Figure 5. Evolution of SSE cycles (a), consisting of pre-slips plus full rupture (b), full rupture with back-propagating fronts (c) and clustered subevents (d) and normal stress distribution with $\lambda = 0.33$ km and $\sigma_A/\sigma_0 = 0.5$. The fitting lines for updip and downdip propagation are in light blue and pink respectively and the corresponding velocity is noted beside (unit: m/s). The threshold slip rate for outlining events is 1×10^{-6} m/s.

3.1.2 Temporal statistics and size distribution

The SSE catalogs simulated on a fault with higher roughness show more randomness and clustering (Figure 4). Figure 4a and d exhibit stable SSE cycles consisting of a full rupture and a partial rupture on a 10 km-long flat fault. However, for the rough fault, Figure 4b and c shows a larger number of SSEs with increasing amplitude of σ perturbations, consistent with the analysis in the previous section. The SSE interevent time catalog for the case with $\sigma_A/\sigma_0 = 0.5$ shows two groups of intervals of about 100 days and 1 hour (Figure 4b), corresponding to the time between full rupture and subsequent cluster, and the time between subevents within pre-slip and subsequent clusters, respectively. However, the case with a higher $\sigma_A/\sigma_0 = 0.96$ exhibits more continuously distributed intervals spanning four orders of magnitude, from 10 minutes to 100 days (Figure 4c), with temporal clustering around the largest events. More small SSEs also appear on faults with higher roughness (Figure 4e and 4f). A cluster of small events can cause less uniform background stress, so the rupture length and time for the next event are less predictable. This result is similar to the observations showing that a large SSE can be decomposed into a cluster of smaller events (Jolivet et al., 2015; Frank, 2016; Frank et al., 2018; Rousset et al., 2019; Jolivet & Frank, 2020).

3.1.3 Rupture velocities

Fault roughness also promotes a range of propagation directions and velocities. Figure 5a shows that one SSE cycle on a rough fault is composed of a cluster of pre-slips (Figure 5b), full rupture (Figure 5c) and clustered subevents (Figure 5d). The dimension of subevents is one to several wavelengths, and they are confined by asperities. The clusters usually start from the boundary of the seismogenic and creeping regions and generally propagate undip intermittently, but sometimes propagate downdip (Figure 5b and 5d). Full ruptures usually nucleate at the end of the cluster of pre-slips (Figure 5b). The updip and downdip propagations of full ruptures exhibit similar velocities: 0.18 and 0.25 m/s (15.5 and 21.6 km/day). However, the propagation velocities of the pre-slip cluster and the subsequent events are smaller than that of the full rupture by a factor of $5-10$. This smaller velocity can be explained by the lower state variable θ: in the cluster of pre-slips and subsequent events, the event in the front is not triggered immediately because it is still below steady-state after the stress change.

3.2 Back propagating fronts

A common feature in rough fault simulations is the occurrence of fast back-propagating fronts within a full rupture (Figure 5c). Their propagation velocity is $3-7$ times higher than the forward propagation. These secondary ruptures may be analogous to rapid tremor reversals (Houston et al., 2011) or fast streaks observed along dip (Shelly et al., 2007; Ghosh et al., 2010).

To understand the origin of back-propagating fronts, in Fig. 6 we compare the evolution of stress and slip velocities on flat and rough faults. On a smooth fault, the crack tip stress and velocity profiles are simply translated as the rupture propagates, and a constant stress drop within the rupture drives the crack at constant velocity (Figure 6a). On the other hand, propagation along rough faults induces large fluctuations in slip velocity and stress drop: the missing piece of the puzzle is a temporary positive stress change $\Delta\tau$ behind the crack tip, that enables ruptured asperities to break again and trigger a secondary slip front. We use the term "delayed stress drop" to describe this mechanism for back-propagating fronts on rough faults, which can be understood in the framework of rate-and-state friction law and velocity-cutoff model. In the case of forward propagation at the crack-tip, the slip rate in the low-σ region is significantly higher than that in the high-σ region (Figure 6d). When the rupture front passes the low-σ region, the slip rate on the asperity behind is also elevated to a similar level as the low-σ region (profile 3 in Figure 6d), which causes the shear stress to increase due to velocity-strengthening behavior at higher slip rate (Figure 1b, profile 3 in Figure 6c). As the rupture propagates into high σ regions, the slip velocity and stress decrease, as shown by the difference between stress profiles 4 and 3 (solid black line in Figure 6c). This delayed stress drop causes a stress increase on the asperities behind ($x \approx 800$ m and $x \approx 1300$ m), and hence induce secondary back propagation in its wave.

3.3 Pulse-to-crack transition and re-rupture on fractal faults

On a fractal fault, heterogeneity varies more randomly than in the sinusoidal cases presented above: since the local amplitude and (to a lesser extent) frequency content varies spatially, the slip regimes displayed in Figure 2 can all coexist on a single fault surface, and slip front propagation across these different regimes generates additional complexity. Figure 7 shows a case with a fractal rough fault with wavelength λ between 0.125 and 10 km and Hurst exponent $H = 0.7$. Within a single full rupture (about one day long), there are two kinds of rupture behaviors, first pulse-like and then crack-like. Additionally, some even faster "streaks" propagate backward in the simulations, analogous to be behavior discussed in section 3.2.

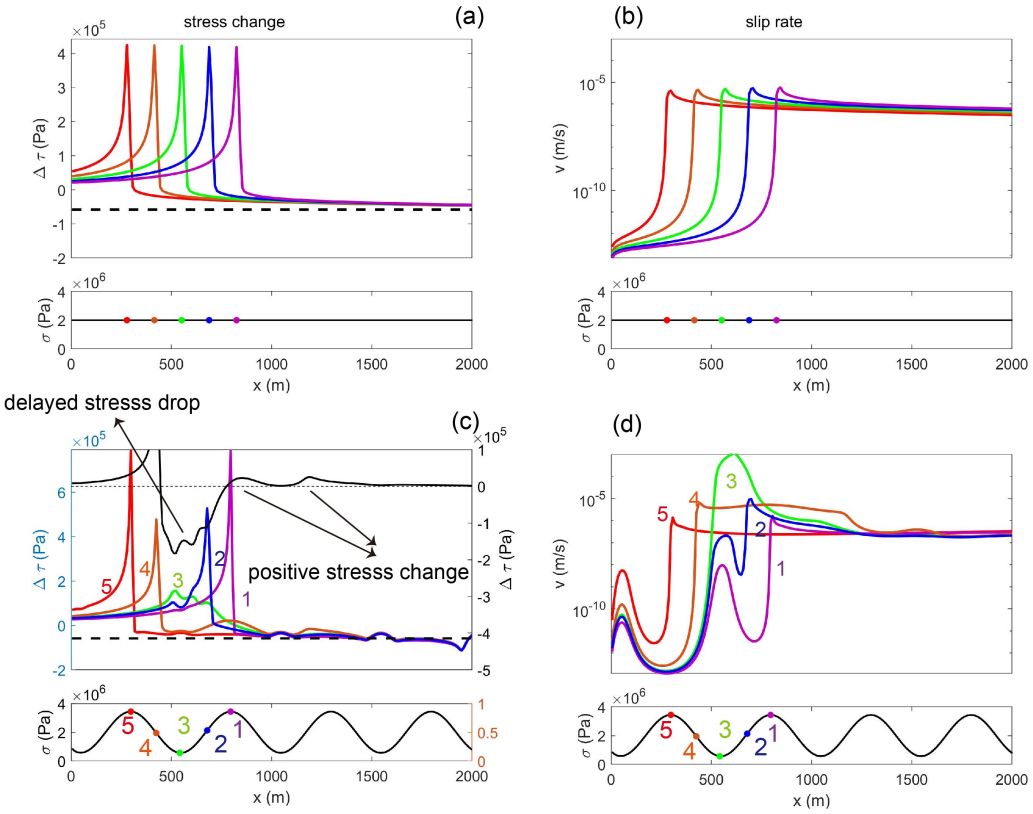

Figure 6. Stress change and slip rate profile along a flat fault (a and b) or fault with sinusoidal normal stress (c and d; $\lambda = 0.5$ km and $\sigma_A/\sigma_0 = 0.71$) when the rupture propagates from right to left. Colored lines represent profiles when the crack tips are at the extrema and mean of σ (c and d; coded by 1 to 5). The black line in (c) represents the difference between stress profiles 4 and 3. The dashed line represents the stress change after an event.

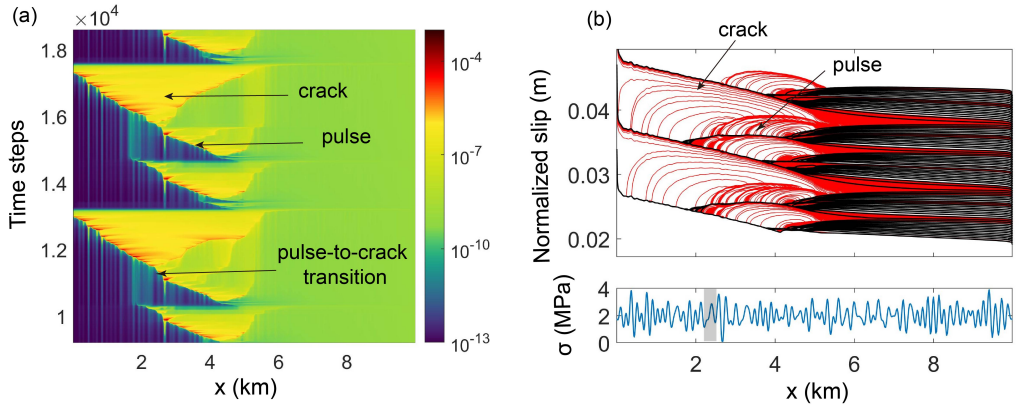

Figure 7. Slip behaviors on a fractal fault. (a) Slip rate across two SSE cycles. (b) Top: normalized slip along the fault during several SSE cycles, (cumulative slip divided by $\frac{\pi}{2} + \arcsin\frac{x-W/2}{W/2}$). The black lines represent interseismic slip with an interval of around 10 days. Red lines are plotted with an interval of 0.25 hour when the maximum slip rate is larger than v_{pl}. Bottom: distribution of the normal stress obtained from Equation 4 with $S = 55$ mm. The grey box denotes where the pulse-to-crack transition happens.

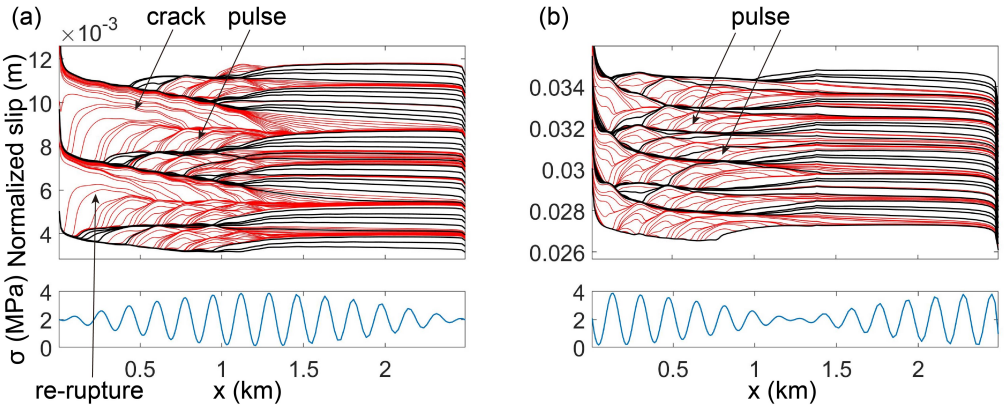

Figure 8. Normalized slip and normal stress for "walnut" case (a) and "hourglass" (b). (a) Re-rupture within a full-rupture event which propagates from high to low roughness regions. (b) SSEs propagating as a pulse from low to high roughness regions without re-rupture.

In Figure 7, pulse-like ruptures are usually clusters of small sub-events and propagate slowly, while crack-like ones are single extensive events and propagate much faster. As shown in section 3.1 and Figure 2, the amplitude of normal stress perturbations determines whether a rupture propagates as a crack or a pulse. Therefore, we proposed that the transition from pulse to crack is caused by spatial variations of normal stress: higher amplitudes of normal stress perturbations favor pulse-like ruptures, so pulse-to-crack transitions can take place as rupture propagates into regions with lower local roughness.

To test this, we compare two end-member cases of a "walnut" and an "hourglass" normal stress perturbation (Figure 8) to study how the local amplitude of the perturbation affects rupture propagation. We construct the normal stress perturbation with two sinusoidal functions of similar wavelengths, 0.179 ($\frac{2.5}{14}$) and 0.167 ($\frac{2.5}{15}$) km, with a group wavelength of 2.5 km. We find that day-long single events exhibit the pulse-to-crack transition and re-rupture in the "walnut" case (Figure 8a), in which the SSE propagates from high roughness to low roughness areas. Ruptures initiate as pulses in the region with a larger perturbation amplitude ($x \approx 1.25$ km) and evolve into cracks in the region with nearly constant normal stress ($x \approx 0$ km). We interpret this as caused by the deficit between crack and pulse-like slip profiles, a mechanism that was previously identified by Idini and Ampuero (2020) for faults surrounded by a damage zone. In principle, the slip deficit could also be filled with subsequent small SSEs as shown in Figure 8b. We suggest that it is also easier for the re-rupture to penetrate the lower-roughness region ($x \approx 0$ km) due to absence of strong asperities, so that a single full rupture is favored. In contrast, ruptures remain pulse-like when propagating from the low into the high roughness region in the "hourglass" case (Figure 8b), which usually last on the order of 10 days. The presence of high normal stress (asperities) in the high roughness region ($x \approx 0$ km) also prevents this area from re-rupturing in a single events, as Figure 8a.

4 Discussion

In this study, we analyze how heterogeneous normal stress induced by fault roughness produces rich slip behavior during slow slip events. We reproduce SSEs with a range of rupture lengths on rough faults in the simulations, which is consistent with geodetic observations that show a power-law distribution of the sizes of slip bursts on a rough fault (Jolivet et al., 2015; Hawthorne & Bartlow, 2018), and is similar to an emerging cascade

of slow slips and foreshocks on rough faults from numerical simulations (Cattania & Segall, 2021). Our simulations also exhibit clustering behaviors that a long-period SSE can be decomposed into several short subevents, which is analogous to the observations such as Frank et al. (2018) and Rousset et al. (2019). We suggest that fault roughness, a universal characteristic in nature, can explain many complex dynamics of SSEs. This complexity can be simply understood within the context of linear elastic fracture mechanics.

Simulations show complex rupture behaviors on rough faults, including forward and back propagation at varying speeds, which differ from that on flat and frictionally uniform faults. We observe strongly-varying slip rates when the rupture front first passes low and high normal stress regions, in contrast to roughly constant slip rate behind back-propagating fronts. The difference can be explained by initial conditions (state variable and slip rate), which are strongly heterogeneous ahead of the rupture front, and more uniform within the rupture itself. Together with a velocity-cutoff model, this varying crack-tip slip rate can also induce a delayed stress drop on the asperity behind, which causes back propagation.

Observations indicate that only certain areas experience repeated RTRs with similar directions, and the propagation velocity differs across locations (Sagae et al., 2023). This points to spatial variations in roughness as a potential reason. Future studies can use the distributions of RTRs, propagation velocity, and high-energy radiators (asperities) to test this hypothesis. Simulations that include a heterogeneous asperities-in-matrix fault also produce back propagation (Luo & Liu, 2021; Peng & Rubin, 2018; Nie & Barbot, 2021). The presence of unstable patches embedded in a stable matrix will produce variations in stress drops when ruptures cross patches with different frictional properties, perhaps analogous to the "delayed stress drop" we observed here. Although our simulations are limited to rate-state friction, the mechanism we identified may also apply to other cases, as long as two conditions are met. The first is the presence of heterogeneous fault properties (such as geometry or friction), capable of efficiently modulating slip rate along the rupture front. The second is a rate-strengthening mechanism, operating on a sufficiently short time scale to allow for fast restrengthening and subsequent stress release upon deceleration, so that a back-propagating front can be triggered. Further studies are need to verify whether other stabilizing mechanisms, such as fault dilatancy (Segall & Rice, 1995), indeed produce similar behavior.

Our simulations show a wide range of propagation velocities. Specifically, the propagation velocity of clustering subevents, forward and back-propagating fronts are on the order of 0.01, 0.1 and 1 m/s, respectively. SSEs generally travel at about 0.1 m/s; however, certain SSEs in Japan and Mexico demonstrate a slower pace of about 0.01 m/s (Gao et al., 2012). Back propagation velocities observed in nature are about $1-5$ and $7-40$ m/s for rapid tremor reversals and along-dip streaks, respectively (Houston et al., 2011; Shelly et al., 2007; Ghosh et al., 2010). While our simulations accurately capture the speeds of forward propagation, they seem to underestimate the back-propagating ones. This implies that the friction parameters in nature are different from those used in our model or that another unknown mechanism controls this process. We will address this problem by exploring a broader region of parameter space and developing theoretical formulas in future studies.

In addition to back-propagating fronts, fractal faults exhibit sustained, large-scale re-ruptures. We have identified a mechanism for this behavior, caused by the more irregular roughness distribution on a fractal fault compared to the sinusoidal case, which can induce pulse-to-crack transitions. Furthermore, natural faults are more complex as the roughness varies spatially on the same surface indicated by the 3D seismic reflection (Kirkpatrick et al., 2020) and Lidar observation (Candela et al., 2009). It is easier to induce re-rupture due to the transition from pulse to crack when SSEs propagate from high roughness to low roughness region. Sagae et al. (2023) shows that the occurrence of sec-

ondary tremor migrations depends on the directions of the primary rupture front. Our mechanism is among the few that offer an explanation for this observation. The pulse-to-crack transition mediated by roughness is not specific to slow slip, and it may be applied to a recently observed "boomerang earthquake", which propagates back through the initial rupture area (Hicks et al., 2020; S. Yamashita et al., 2022).

5 Conclusion

We find clustering of slow slip events, different rupture lengths, and varying propagation velocities on a rough fault in the simulations. SSEs tend to arrest and propagate intermittently, which generates a pulse-like slip profile when roughness is high, and the amplitude of the normal stress perturbation is large. The secondary back propagation can be induced by fault restrengthening followed by a delayed stress drop when the rupture passes a low normal stress region. Finally, we find that the transition from pulse to crack can lead to a large scale re-rupture and back propagation when SSEs propagate from high to low roughness regions on a fractal fault.

Acknowledgments
The authors thank Jared Bryan, Xin Cui, William Frank, Zhi Li, Enrico Milanese, and Qing-Yu Wang for helpful discussions. Y.S. received fundings from MIT EAPS Robert R Shrock Fellowship, Sven Treitel (1953) Fellowship, and MIT Mathworks Fellowship.

Appendix A Estimating propagation velocities

To calculate propagation velocity, we used two methods: one for a single event, and one for clusters of several events. The first method is to use a slip rate threshold to outline events and fit the rupture fronts linearly to calculate updip and downdip propagation velocity (e.g. full rupture in Figure 5b). We can also increase the threshold to delineate the back-propagating fronts and calculate their velocities. We may not capture all the back-propagating fronts using one threshold, so we use several thresholds and choose the most representative velocity by visual inspection.

Figure 2f also shows clusters of intermittent events that produce a "fish-scale" pattern with each event arresting on a high normal-stress patch. To estimate the propagation velocity of these clusters, we first outline the subevents by a threshold near the cut-off velocity (1×10^{-6} m/s). Then we identify clusters as groups of subevents with the interevent time less than 3 days, which separates the two peaks of the bimodal inter-event time distribution in Figure 4b. Finally, we use the uppermost/lowermost end of every event to calculate the updip/downdip propagation velocity of the cluster (e.g. pre-slips in Figure 5b and subsequent events in Figure 5d).

Appendix B Criterion for rupture propagation and arrest

In Figure 2, ruptures show pulse-like behavior and stop in high-σ region because the local toughness there is higher. Here we present a fracture mechanics analysis to explain rupture propagation and arrest under heterogeneous normal stress. For simplicity, we neglect rupture arrest caused by gradients in the background stress field due to loading from deep creep (Cattania, 2019). SSEs are mostly nucleated at peaks of normal stress, so we consider a crack extending from the normal stress maximum at $x = 0$ (eq. 5) to the crack tip at $x = l$ to obtain stress intensity factor K (Tada et al., 1973) as a function of the stress drop $\Delta\tau$:

$$K = \int_0^l \frac{\sqrt{2}}{\sqrt{\pi(l-x)}}\Delta\tau(x)dx = 2\sqrt{\frac{2l}{\pi}}\Delta\tau_0 + \sqrt{\frac{2\lambda}{\pi}}\Delta\tau_A\left[C(2\sqrt{\frac{l}{\lambda}})\cos\frac{2\pi l}{\lambda} + S(2\sqrt{\frac{l}{\lambda}})\sin\frac{2\pi l}{\lambda}\right],$$

$$S(x) = \int_0^x \sin\frac{\pi t^2}{2}dt,$$

$$C(x) = \int_0^x \cos \frac{\pi t^2}{2} dt, \tag{B1}$$

where $S(x)$ and $C(x)$ are Fresnel integrals. In Equation B1, $\Delta\tau$ is assumed proportional to normal stress (Equation 5), with $\Delta\tau_0$ and $\Delta\tau_A$ due to the constant and sinusoidal terms respectively. The stress drop equals the difference between the initial and minimum frictional stress as:

$$\Delta\tau_{0,A} = \sigma_{0,A} \left(-a \ln \frac{v_{\tau-min}}{v_i} + b \ln \frac{v_c \theta_i / D_c + 1}{v_c / v_{\tau-min} + 1} \right), \tag{B2}$$

where v_i and θ_i are the initial slip rate and initial state variable, respectively. In simulations, the slip rate is $v_i \approx v_{pl}$ in the nucleation zone and it is near steady state as $v_i \theta_i / D_c = 1$.

The local toughness K_c is calculated from the fracture energy G_c as $G_c = \frac{K_c^2}{2G'} = \frac{D_c}{2b\sigma}(\Delta\tau_{p-r})^2$, where $\Delta\tau_{p-r}$ is the peak to residual stress drop. Hawthorne and Rubin (2013a) derived the stress drop for the velocity-cutoff model as

$$\Delta\tau_{p-r} = b\sigma \left[\ln \left(\frac{v_c \theta_i / 2}{D_c} + 1 \right) - \ln \left(\frac{v_c}{v_{max}/2} + 1 \right) \right]. \tag{B3}$$

Thus, K_c is given by

$$K_c = \sqrt{G' b \sigma D_c} \left[\ln \left(\frac{v_c \theta_i / 2}{D_c} + 1 \right) - \ln \left(\frac{v_c}{v_{max}/2} + 1 \right) \right]. \tag{B4}$$

To simplify, we use $\theta_i = D_c / v_{pl}$, which represents the creeping region, for K_c all along the fault. This choice is made because K and K_c have a phase difference of about $\pi/2$, with the second zero crossing frequently occurring within the creeping region (Figure 3). Additionally, both the high and low-σ regions undergo creeping following the first rupture.

Open Research Section

We use MATLAB to plot figures. The results of our simulations (Figure 2, 5 and 7) and simulated SSE catalogs (Figure 4) are archived in Zenodo (Sun & Cattania, 2024).

References

Ampuero, J.-P., & Rubin, A. M. (2008). Earthquake nucleation on rate and state faults–aging and slip laws. *Journal of Geophysical Research: Solid Earth*, *113*(B1).

Audet, P., & Kim, Y. (2016). Teleseismic constraints on the geological environment of deep episodic slow earthquakes in subduction zone forearcs: A review. *Tectonophysics*, *670*, 1–15.

Bartlow, N. M., Miyazaki, S., Bradley, A. M., & Segall, P. (2011). Space-time correlation of slip and tremor during the 2009 cascadia slow slip event. *Geophysical Research Letters*, *38*(18).

Behr, W. M., & Bürgmann, R. (2021). What's down there? the structures, materials and environment of deep-seated slow slip and tremor. *Philosophical Transactions of the Royal Society A*, *379*(2193), 20200218.

Behr, W. M., Gerya, T. V., Cannizzaro, C., & Blass, R. (2021). Transient slow slip characteristics of frictional-viscous subduction megathrust shear zones. *AGU Advances*, *2*(3), e2021AV000416.

Bletery, Q., & Nocquet, J.-M. (2020). Slip bursts during coalescence of slow slip events in cascadia. *Nature communications*, *11*(1), 1–6.

Bletery, Q., Thomas, A. M., Hawthorne, J. C., Skarbek, R. M., Rempel, A. W., & Krogstad, R. D. (2017). Characteristics of secondary slip fronts associated with slow earthquakes in cascadia. *Earth and Planetary Science Letters*, *463*, 212–220.

Brodsky, E. E., Kirkpatrick, J. D., & Candela, T. (2016). Constraints from fault roughness on the scale-dependent strength of rocks. *Geology*, *44*(1), 19–22.

Candela, T., Renard, F., Bouchon, M., Brouste, A., Marsan, D., Schmittbuhl, J., & Voisin, C. (2009). Characterization of fault roughness at various scales: Implications of three-dimensional high resolution topography measurements. In *Mechanics, structure and evolution of fault zones* (pp. 1817–1851). Springer.

Candela, T., Renard, F., Klinger, Y., Mair, K., Schmittbuhl, J., & Brodsky, E. E. (2012). Roughness of fault surfaces over nine decades of length scales. *Journal of Geophysical Research: Solid Earth*, *117*(B8).

Cattania, C. (2019). Complex earthquake sequences on simple faults. *Geophysical Research Letters*, *46*(17-18), 10384–10393.

Cattania, C., & Segall, P. (2021). Precursory slow slip and foreshocks on rough faults. *Journal of Geophysical Research: Solid Earth*, *126*(4), e2020JB020430.

Cruz-Atienza, V. M., Villafuerte, C., & Bhat, H. S. (2018). Rapid tremor migration and pore-pressure waves in subduction zones. *Nature communications*, *9*(1), 1–13.

Erickson, B. A., Jiang, J., Lambert, V., Barbot, S. D., Abdelmeguid, M., Almquist, M., ... others (2023). Incorporating full elastodynamic effects and dipping fault geometries in community code verification exercises for simulations of earthquake sequences and aseismic slip (seas). *Bulletin of the Seismological Society of America*, *113*(2), 499–523.

Eshelby, J. D. (1957). The determination of the elastic field of an ellipsoidal inclusion, and related problems. *Proceedings of the royal society of London. Series A. Mathematical and physical sciences*, *241*(1226), 376–396.

Fang, Z., & Dunham, E. M. (2013). Additional shear resistance from fault roughness and stress levels on geometrically complex faults. *Journal of Geophysical Research: Solid Earth*, *118*(7), 3642–3654.

Frank, W. B. (2016). Slow slip hidden in the noise: The intermittence of tectonic release. *Geophysical Research Letters*, *43*(19), 10–125.

Frank, W. B., Rousset, B., Lasserre, C., & Campillo, M. (2018). Revealing the cluster of slow transients behind a large slow slip event. *Science advances*, *4*(5), eaat0661.

Gao, H., Schmidt, D. A., & Weldon, R. J. (2012). Scaling relationships of source parameters for slow slip events. *Bulletin of the Seismological Society of America*, *102*(1), 352–360.

Ghosh, A., Vidale, J. E., Sweet, J. R., Creager, K. C., Wech, A. G., Houston, H., & Brodsky, E. E. (2010). Rapid, continuous streaking of tremor in cascadia. *Geochemistry, Geophysics, Geosystems*, *11*(12).

Griffith, A. A. (1921). Vi. the phenomena of rupture and flow in solids. *Philosophical transactions of the royal society of london. Series A, containing papers of a mathematical or physical character*, *221*(582-593), 163–198.

Hawthorne, & Bartlow, N. (2018). Observing and modeling the spectrum of a slow slip event. *Journal of Geophysical Research: Solid Earth*, *123*(5), 4243–4265.

Hawthorne, Bostock, M. G., Royer, A. A., & Thomas, A. M. (2016). Variations in slow slip moment rate associated with rapid tremor reversals in c ascadia. *Geochemistry, Geophysics, Geosystems*, *17*(12), 4899–4919.

Hawthorne, & Rubin, A. (2013a). Laterally propagating slow slip events in a rate and state friction model with a velocity-weakening to velocity-strengthening transition. *Journal of Geophysical Research: Solid Earth*, *118*(7), 3785–3808.

Hawthorne, & Rubin, A. M. (2013b). Tidal modulation and back-propagating fronts in slow slip events simulated with a velocity-weakening to velocity-strengthening friction law. *Journal of Geophysical Research: Solid Earth*, *118*(3), 1216–1239.

Heimisson, E. R. (2020). Crack to pulse transition and magnitude statistics during earthquake cycles on a self-similar rough fault. *Earth and Planetary Science Letters*, *537*, 116202.

Hicks, S. P., Okuwaki, R., Steinberg, A., Rychert, C. A., Harmon, N., Abercrombie, R. E., ... others (2020). Back-propagating supershear rupture in the 2016 mw 7.1 romanche transform fault earthquake. *Nature Geoscience*, *13*(9), 647–653.

Houston, H., Delbridge, B. G., Wech, A. G., & Creager, K. C. (2011). Rapid tremor reversals in cascadia generated by a weakened plate interface. *Nature Geoscience*, *4*(6), 404–409.

Idini, B., & Ampuero, J.-P. (2020). Fault-zone damage promotes pulse-like rupture and back-propagating fronts via quasi-static effects. *Geophysical Research Letters*, *47*(23), e2020GL090736.

Ikari, M. J., & Saffer, D. M. (2011). Comparison of frictional strength and velocity dependence between fault zones in the nankai accretionary complex. *Geochemistry, Geophysics, Geosystems*, *12*(4).

Im, K., Saffer, D., Marone, C., & Avouac, J.-P. (2020). Slip-rate-dependent friction as a universal mechanism for slow slip events. *Nature Geoscience*, *13*(10), 705–710.

Irwin, G. R. (1957). Analysis of stresses and strains near the end of a crack traversing a plate.

Jolivet, R., Candela, T., Lasserre, C., Renard, F., Klinger, Y., & Doin, M.-P. (2015). The burst-like behavior of aseismic slip on a rough fault: The creeping section of the haiyuan fault, china. *Bulletin of the Seismological Society of America*, *105*(1), 480–488.

Jolivet, R., & Frank, W. (2020). The transient and intermittent nature of slow slip. *AGU Advances*, *1*(1), e2019AV000126.

Kirkpatrick, J. D., Edwards, J. H., Verdecchia, A., Kluesner, J. W., Harrington, R. M., & Silver, E. A. (2020). Subduction megathrust heterogeneity characterized from 3d seismic data. *Nature Geoscience*, *13*(5), 369–374.

Kirkpatrick, J. D., Fagereng, Å., & Shelly, D. R. (2021). Geological constraints on the mechanisms of slow earthquakes. *Nature Reviews Earth & Environment*, *2*(4), 285–301.

Lavier, L. L., Bennett, R. A., & Duddu, R. (2013). Creep events at the brittle ductile transition. *Geochemistry, Geophysics, Geosystems*, *14*(9), 3334–3351.

Lay, T., Kanamori, H., Ammon, C. J., Koper, K. D., Hutko, A. R., Ye, L., ... Rushing, T. M. (2012). Depth-varying rupture properties of subduction zone megathrust faults. *Journal of Geophysical Research: Solid Earth*, *117*(B4).

Liu, Y., & Rice, J. R. (2005). Aseismic slip transients emerge spontaneously in three-dimensional rate and state modeling of subduction earthquake sequences. *Journal of Geophysical Research: Solid Earth*, *110*(B8).

Liu, Y., & Rice, J. R. (2007). Spontaneous and triggered aseismic deformation transients in a subduction fault model. *Journal of Geophysical Research: Solid Earth*, *112*(B9).

Luo, Y., & Ampuero, J.-P. (2018). Stability of faults with heterogeneous friction properties and effective normal stress. *Tectonophysics*, *733*, 257–272.

Luo, Y., & Liu, Z. (2021). Fault zone heterogeneities explain depth-dependent pattern and evolution of slow earthquakes in cascadia. *Nature communications*, *12*(1), 1–13.

Marone, C. (1998). Laboratory-derived friction laws and their application to seismic faulting. *Annual Review of Earth and Planetary Sciences*, *26*(1), 643–696.

Michel, S., Gualandi, A., & Avouac, J.-P. (2019). Similar scaling laws for earthquakes and cascadia slow-slip events. *Nature*, *574*(7779), 522–526.

Nie, S., & Barbot, S. (2021). Seismogenic and tremorgenic slow slip near the stability transition of frictional sliding. *Earth and Planetary Science Letters*, *569*, 117037.

Obara, K., Hirose, H., Yamamizu, F., & Kasahara, K. (2004). Episodic slow slip events accompanied by non-volcanic tremors in southwest japan subduction zone. *Geophysical Research Letters*, *31*(23).

Obara, K., Matsuzawa, T., Tanaka, S., & Maeda, T. (2012). Depth-dependent mode of tremor migration beneath kii peninsula, nankai subduction zone. *Geophysical Research Letters*, *39*(10).

Peng, & Gomberg, J. (2010). An integrated perspective of the continuum between earthquakes and slow-slip phenomena. *Nature geoscience*, *3*(9), 599–607.

Peng, & Rubin, A. M. (2018). Simulating short-term evolution of slow slip influenced by fault heterogeneities and tides. *Geophysical Research Letters*, *45*(19), 10–269.

Power, W., Tullis, T., Brown, S., Boitnott, G., & Scholz, C. (1987). Roughness of natural fault surfaces. *Geophysical Research Letters*, *14*(1), 29–32.

Power, W. L., & Tullis, T. E. (1991). Euclidean and fractal models for the description of rock surface roughness. *Journal of Geophysical Research: Solid Earth*, *96*(B1), 415–424.

Radiguet, M., Cotton, F., Vergnolle, M., Campillo, M., Valette, B., Kostoglodov, V., & Cotte, N. (2011). Spatial and temporal evolution of a long term slow slip event: the 2006 guerrero slow slip event. *Geophysical Journal International*, *184*(2), 816–828.

Renard, F., & Candela, T. (2017). Scaling of fault roughness and implications for earthquake mechanics. *Fault zone dynamic processes: Evolution of fault properties during seismic rupture*, *227*, 197–216.

Rice, J. R. (1993). Spatio-temporal complexity of slip on a fault. *Journal of Geophysical Research: Solid Earth*, *98*(B6), 9885–9907.

Rogers, G., & Dragert, H. (2003). Episodic tremor and slip on the cascadia subduction zone: The chatter of silent slip. *Science*, *300*(5627), 1942–1943.

Romanet, P., Sato, D. S., & Ando, R. (2020). Curvature, a mechanical link between the geometrical complexities of a fault: application to bends, kinks and rough faults. *Geophysical Journal International*, *223*(1), 211–232.

Rousset, B., Fu, Y., Bartlow, N., & Bürgmann, R. (2019). Weeks-long and years-long slow slip and tectonic tremor episodes on the south central alaska megathrust. *Journal of Geophysical Research: Solid Earth*, *124*(12), 13392–13403.

Rubin, A. M. (2008). Episodic slow slip events and rate-and-state friction. *Journal of Geophysical Research: Solid Earth*, *113*(B11).

Rubin, A. M., & Ampuero, J.-P. (2005). Earthquake nucleation on (aging) rate and state faults. *Journal of Geophysical Research: Solid Earth*, *110*(B11).

Ruina, A. (1983). Slip instability and state variable friction laws. *Journal of Geophysical Research: Solid Earth*, *88*(B12), 10359–10370.

Saffer, D. M., Frye, K. M., Marone, C., & Mair, K. (2001). Laboratory results indicating complex and potentially unstable frictional behavior of smectite clay. *Geophysical Research Letters*, *28*(12), 2297–2300.

Sagae, K., Nakahara, H., Nishimura, T., & Imanishi, K. (2023). Fine structure of tremor migrations beneath the kii peninsula, southwest japan, extracted with a space-time hough transform. *Journal of Geophysical Research: Solid Earth*, *128*(6), e2022JB026248.

Segall, P., & Bradley, A. M. (2012). Slow-slip evolves into megathrust earthquakes in 2d numerical simulations. *Geophysical Research Letters*, *39*(18).

Segall, P., & Rice, J. R. (1995). Dilatancy, compaction, and slip instability of a fluid-infiltrated fault. *Journal of Geophysical Research: Solid Earth*, *100*(B11), 22155–22171.

Segall, P., Rubin, A. M., Bradley, A. M., & Rice, J. R. (2010). Dilatant strengthening as a mechanism for slow slip events. *Journal of Geophysical Research: Solid Earth*, *115*(B12).

Shelly, D. R., Beroza, G. C., & Ide, S. (2007). Complex evolution of transient slip derived from precise tremor locations in western shikoku, japan. *Geochemistry, Geophysics, Geosystems*, *8*(10).

Sun, Y., & Cattania, C. (2024, April). *Simulation Results in the Paper "Propagation of Slow Slip Events on Rough Faults: Clustering, Back Propagation, and Re-rupturing" [Dataset].* Zenodo. Retrieved from `https://doi.org/10.5281/zenodo.10988744` doi: 10.5281/zenodo.10988744

Tada, H., Paris, P. C., & Irwin, G. R. (1973). The stress analysis of cracks. *Handbook, Del Research Corporation*, *34*.

Wallace, L. M. (2020). Slow slip events in new zealand. *Annual Review of Earth and Planetary Sciences*, *48*, 175–203.

Wech, A. G., & Bartlow, N. M. (2014). Slip rate and tremor genesis in cascadia. *Geophysical Research Letters*, *41*(2), 392–398.

Yamashita, Yakiwara, H., Asano, Y., Shimizu, H., Uchida, K., Hirano, S., ... others (2015). Migrating tremor off southern kyushu as evidence for slow slip of a shallow subduction interface. *Science*, *348*(6235), 676–679.

Yamashita, S., Yagi, Y., & Okuwaki, R. (2022). Irregular rupture propagation and geometric fault complexities during the 2010 mw 7.2 el mayor-cucapah earthquake. *Scientific reports*, *12*(1), 1–10.

Yin, A. (2018). Water hammers tremors during plate convergence. *Geology*, *46*(12), 1031–1034.

Yin, A., Xie, Z., & Meng, L. (2018). A viscoplastic shear-zone model for deep (15–50 km) slow-slip events at plate convergent margins. *Earth and Planetary Science Letters*, *491*, 81–94.